Macromolecular Research

Article

DOI 10.1007/s13233-021-9100-x

www.springer.com/13233 pISSN 1598-5032 eISSN 2092-7673

Fullerene-Based Photoactive A-D-A Triads for Single-Component Organic Solar Cells: Incorporation of Non-Fused Planar Conjugated Core

Young Woong Lee[†,1]
Jiwoo Yeop[†,2]
Jin Young Kim[*,2]
Han Young Woo[*,1]

[1] Department of Chemistry, Korea University, Anam-ro 145, Seoul 02841, Korea
[2] Department of Energy Engineering, Ulsan National Institute of Science and Technology (UNIST), Ulsan 44919, Korea

Received September 24, 2021 / Revised November 12, 2021 / Accepted November 16, 2021

Abstract: Two acceptor-donor-acceptor (A-D-A) single-component (SC) photovoltaic triad molecules, P3T4Rh-C_6-PC_{61}BM and P3T4Rh-C_{10}-PC_{61}BM, were synthesized. A conformation-locked planar conjugated core, 1,4-bis(thiophenylphenylthiophene)-2,5-difluorophenylene (P3T4), with intrachain noncovalent coulombic interactions was coupled with two fullerene derivatives, [6,6]-phenyl-C61 butyric acid propargyl ester, *via* copper (I)-catalyzed azide-alkyne 1,3-dipolar cycloaddition. The D-A separation was varied by modulating the spacer alkyl chain length (C6 and C10). Both SC triads exhibited maximum absorption by the P3T4 core at λ_{abs} = 507-510 nm, as well as absorption by PC_{61}BM at ~300 nm. Because of the broken conjugation between the P3T4 core and PC_{61}BM termini, the highest occupied molecular orbital (-5.58 to -5.59 eV) was determined by the P3T4 moiety, and the lowest unoccupied molecular orbital (-3.89 to -3.92 eV) was determined by PC_{61}BM in the SC structures. In diluted solution, both SC triads showed significant photoluminescence quenching, indicating efficient intramolecular charge transfer between the P3T4 and PC_{61}BM moieties. However, the semicrystalline packing of the P3T4 core was severely disrupted by the incorporation of a bulky PC_{61}BM moiety at each terminus, which degraded the carrier transport and diode characteristics of SC organic solar cells (SCOSCs) based on P3T4Rh-C_6-PC_{61}BM and P3T4Rh-C_{10}-PC_{61}BM, as indicated by poor power conversion efficiency (~0.4%). No clear spacer length effect was observed. To improve the performance of SCOSCs, a design strategy is needed that enhances the intermolecular packing and ordering of the D and A moieties, which are important prerequisites for the development of optimal SC photoactive molecules.

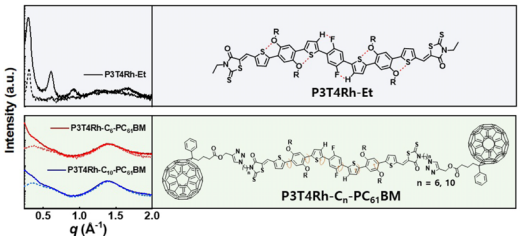

Keywords: organic solar cells, organic photovoltaics, single component organic solar cells, fullerene-based triads, thin film morphology.

1. Introduction

Organic solar cells (OSCs) have been intensively studied over the last two decades because of advantages including high absorptivity, low-cost solution processibility, and mechanical flexibility, which endows bulk heterojunction (BHJ) donor/acceptor (D/A) blended OSCs with power conversion efficiencies (PCEs) above 17%-18%.[1-8] Single-component (SC) OSCs (SCOSCs) have also attracted increasing attention recently as devices with excellent potential for simplifying the design of BHJ OSCs.[9,10] SC photoelectric materials are adopted as the active layer in SCOSCs, where D and A moieties are chemically linked by a covalent bond. Compared to BHJ systems, well-designed SC materials can afford a simpler fabrication process for optimal devices with reduced device-to-device variation. Because the D and A moieties are chemically bonded, morphological changes (i.e., D and A phase separation) during device operation can be suppressed compared to those in BHJ OSCs.[11-15]

Various molecular designs for photoactive materials for use in SCOSCs have been reported, including SC photovoltaic polymers and small molecules. Remarkable advances in SC systems based on double-cable polymers and conjugated block copolymers (BCPs) have been reported recently, with maximum PCEs of 8.4% and 11.32%, respectively.[16-22] Cravino and Sariciftci first proposed the concept of double-cable polymers using a p-type polymer as a hole-transport channel (p-cable) with covalently dangled n-type structures as pendants for an electron-transport channel (n-cable).[23] Li and co-workers recently developed several nonfullerene-based double-cable polymers using naphthalene diimide (NDI) and perylene diimide as n-type pendant units.[16,21,24-29] A new SC photovoltaic polymer, JP02, was designed with precisely controlled miscibility between a polymer backbone and dangling NDI units by adjusting the substitution position of the Cl atom on the polymer backbone.[16] Because of the enhanced miscibility, exciton separation, and charge carrier mobility of JP02, SCOSCs employing JP02 as a photoactive layer achieved remarkably high PCEs of up to 8.4%, as well as a high external quantum efficiency (EQE) and a fill factor (FF) of >0.70. For the development of SCOSCs based on conjugated BCPs, Choi

Acknowledgments: This work was financially supported by the National Research Foundation (NRF) of Korea (Grants NRF-2019R1A2C2085290, 2019R1A6A1A11044070, 2020M3H4A3081814). We thank the Institute for Basic Science (IBS) Center for Molecular Spectroscopy and Dynamics (IBS-R023-D1) for providing (NMR Spectrometry) and professional technical support.

***Corresponding Authors:** Han Young Woo (hywoo@korea.ac.kr), Jin Young Kim (jykim@unist.ac.kr)
[†]These authors equally contributed to this work.

developed a facile one-pot copolymerization method for synthesizing conjugated BCPs (PBDT2T-*b*-N220) and obtained a PCE of 6.43%, where p- and n-type semiconducting oligomer blocks were conjugated in the one-pot reaction without requiring the isolation of each oligomeric unit.[19,20] The one-pot copolymerization method enables the use of a wide range of building blocks for the design of BCPs.[17,18] Min recently reported a PCE of 11.32% for an SCOSC device using PBDB-T-*b*-PYT, which was synthesized by one-pot polymerization using PBDB-T and PYT as the D and A blocks, respectively.[17] 1-Chloronaphthalene (CN) additive treatment of the PBDB-T-*b*-PYT film significantly enhanced the face-on orientation and improved the π-π and lamellar stacking of the polymers. The increase in crystalline domains after CN treatment significantly improved both the short-circuit current density (J_{SC}, from 16.90 to 19.60 mA cm^{-2}) and FF (from 0.46 to 0.63).

By contrast, the development of small-molecule-based SCOSCs is far behind that of their polymeric counterparts.[13,30-35] Bäuerle reported a series of D-A dyads based on oligothiophene and fullerene derivatives as D and A moieties with controlled D-A spacing.[33-35] Solvent vapor annealing (SVA) caused the efficient crystallization of the D moieties with a short ethyl linker and yielded a PCE of 4.26% and 5.34% for the SC materials using [6,6]-phenyl-C61 butyric acid methyl ester ($PC_{61}BM$) and [6,6]-phenyl-C71 butyric acid methyl ester as respective A moieties, which is the highest reported for small-molecule-based SCOSC devices. In addition, several research groups have attempted to develop A-D-A triad-type SC materials, which exhibit increased light absorption because of the controlled D/A ratio. For fullerene OSCs, the absorption coefficient of the A moiety (fullerene derivatives) is lower than that of the D moiety (p-type organic semiconductors), and thus a higher concentration of the A moiety compared to the D moiety is needed to optimize the photovoltaic properties of D/A BHJ OSCs.[36] We reported an oligothiophene-based A-D-A-type triad (BDTRh-PCBM) SCOSC that uses a fused benzo[1,2-b:4,5-b]dithiophene (BDT)-based core with a fullerene acceptor at each terminus and showed a PCE of 2.44%.[31] The design of optimized A-D-A triad-type fullerene-based SC molecules is quite challenging because the bulky fullerene units on both sides strongly inhibit the crystallization of the D moieties. According to the recent SCOSC studies discussed above, the crystalline packing of D and A moieties in the film, which determines the formation of bi-continuous charge transport pathways, clearly has dramatic effects on solar cell efficiency. To increase the intermolecular packing despite disruption by the bulky terminal fullerene moieties, the D core should be designed carefully, which is still a challenge in the development of ideal SC photovoltaic materials.

In this study, we synthesized two A-D-A-type SC photoactive triads (P3T4Rh-C_6-$PC_{61}BM$ and P3T4Rh-C_{10}-$PC_{61}BM$) based on a 1,4-bis(thiophenylphenylthiophene)-2,5-difluorophenylene (P3T4) core, which was designed to have planar structure with conformation locking *via* noncovalent coulombic interactions along the conjugated backbone. A $PC_{61}BM$ moiety was incorporated at each terminus, and the spacer length was varied (C6 and C10 in P3T4Rh-C_6-$PC_{61}BM$ and P3T4Rh-C_{10}-$PC_{61}BM$, respectively). The role of the conjugated core in the SC triad structures is very important in determining the semicrystalline intermolecular packing, carrier transport, and photovoltaic properties of the SCOSCs. The optical, electrochemical, morphological, and photoelectrical characteristics of the two SC photoactive materials are investigated in detail.

2. Experimental

2.1. General

^{1}H and ^{13}C nuclear magnetic resonance (NMR) spectra were recorded using a Bruker Advance III HD system operating at 500 MHz and 125 MHz, respectively. UV-vis spectra were obtained using a JASCO (V-630) spectrophotometer. Cyclic voltammetry data were measured using a Versa STAT3 (Princeton Applied Research) with a three-electrode cell in 0.1 M tetrabutylammonium tetrafluoroborate (Bu_4NBF_4) in acetonitrile at a scan rate of 50 mV/s. Differential scanning calorimetry (DSC) and thermogravimetric analysis (TGA) were performed by DSC 4000 (PerkinElmer) and TGA N-1000 (Scinco), respectively, with a heating and cooling rate of 10 ℃ min^{-1} under nitrogen (purity, 99.999%). Grazing-incidence wide-angle X-ray scattering (GIWAXS) measurements were carried out at the Pohang Accelerator Laboratory (beam energy: 11.03 keV, X-ray wavelength: 1.124 Å and the incident angle: 0.12°), Pohang, Republic of Korea. Atomic Force Microscopy (AFM) images were measured in tapping mode, using XE-100 from Park Systems. High-resolution mass (HRMS) spectroscopy using matrix-assisted laser desorption ionization time-of-flight (MALDI-TOF) was performed by MALDI-TOF/TOF 5800 system (AB SCIEX) using 2,5-dihydroxybenzoic acid as matrix.

2.2. OPV fabrication

The devices were fabricated using a solution process with a conventional structure of indium tin oxide (ITO)/poly(3,4-ethylenedioxythiophene):polystyrene sulfonate (PEDOT:PSS)/active layer/ZnO nanoparticles/Al. An ITO-coated glass was cleaned by ultrasonication in deionized water, acetone, and isopropyl alcohol for 10 min, respectively. The dried ITO glass was subjected to UV-ozone treatment for 30 min. PEDOT:PSS as hole transport layer was spin-coated on the top of ITO glass at 4000 rpm for 40 s. After drying at 140 ℃ for 10 min, it was transferred to a glovebox filled with nitrogen gas. The SC molecules P3T4Rh-C_n-$PC_{61}BM$ (n = 6, 10) were dissolved in chlorobenzene (CB, 20 mg/mL) with the solvent additive of diphenyl ether (DPE, 1 vol%) and spin-coated onto the PEDOT:PSS layer at 4000 rpm for 40 s. ZnO nanoparticles dissolved in methanol (MeOH, 5 mg/mL) were spin-coated as an electron transport layer on the active layer at 4000 rpm for 40 s. The devices were pumped down in the vacuum (<10^{-6} torr), and 100 nm thick Al electrode was deposited on top of the active layer. The deposited Al electrode area defined the active area of the devices as 4.0 mm^2. The measurements of photovoltaic characteristics were performed inside a glove box using a high quality of optical fiber to guide the light from the solar simulator equipped with a Keithley 2635A source measurement unit. The current density-voltage (J-V) characteristics for the devices were measured under AM 1.5 G illumination at 100 mW/cm^2. The incident photon to current conversion efficiency (IPCE) measurements were carried out in ambient

air using an IPCE system (Model QEX7) by PV measurements Inc. (Boulder, Colorado).

2.3. Materials and synthesis

All the chemical reagents were purchased from Sigma Aldrich and Tokyo Chemical Industry and used as received without further purification. P3T4-CHO was synthesized according to the previously reported procedures.[37]

2.3.1. 3-(6-Hydroxyhexyl)rhodanine (1a)

A suspension of 6-amino-1-hexanol (2.00 g, 17.1 mmol) and bis(carboxymethyl)trithiocarbonate (4.25 g, 18.8 mmol) in water was reacted in a microwave reactor at 150 ℃ for 1 h and the generated fume was ventilated. After cooled to room temperature, the reaction solution was extracted with ethyl acetate (EA) three times. Organic phase was collected and dried with anhydrous magnesium sulfate ($MgSO_4$). After removing the solvent by rotary evaporation, the concentrated solution was purified by column chromatography using chloroform (CF):EA (7:3 by volume) as eluent, yielding a pale-yellow viscous liquid (0.80 g, 20.2%). ^{1}H NMR (500 MHz, $CDCl_3$): δ (ppm) 3.98 (t, 2H), 3.97 (s, 2H), 3.64 (t, 2H), 1.68-1.62 (m, 2H), 1.60-1.54 (m, 2H), 1.43-1.35 (m, 4H). ^{13}C NMR (125 MHz, $CDCl_3$): δ (ppm) 201.26, 174.02, 62.79, 44.62, 35.37, 32.33, 26.63, 26.32, 25.19.

2.3.2. 3-(10-Hydroxydecyl)rhodanine (1b)

Compound 1b was synthesized by following the procedure for compound 1a using 10-amino-1-decanol (2.96 g, 17.1 mmol) and bis(carboxymethyl)trithiocarbonate (4.25 g, 18.8 mmol). Yield: 1.24 g (25.0%). ^{1}H NMR (500 MHz, $CDCl_3$): δ (ppm) 3.97 (t, 2H), 3.96 (s, 2H), 3.64 (q, 2H), 1.64-1.61 (m, 2H), 1.58-1.53 (m, 2H), 1.37-1.21 (m, 12H). ^{13}C NMR (125 MHz, $CDCl_3$): δ (ppm) 201.32, 173.98, 62.90, 44.76, 35.40, 32.74, 29.44, 29.35, 29.32, 29.06, 26.69, 26.65, 25.70.

2.3.3. 3-(6-(4-Toluenesulfonate)hexyl)rhodanine (2a)

A solution of compound 1a (0.80 g, 3.45 mmol), and pyridine (2.73 g, 34.5 mmol) in anhydrous CF was cooled to 0 ℃. 4-Toluenesulfonyl chloride (0.724 g, 3.80 mmol) was dissolved in anhydrous CF and transferred to a reaction solution dropwise with stirring for 30 min. The reaction solution was warmed to room temperature with stirring for 2 h. The organic phase was collected by extraction with CF three times and dried over anhydrous $MgSO_4$. After removing the solvent using rotary evaporation, the concentrated crude product was purified by silica gel column chromatography with CF:EA (9:1 by volume) as eluent, yielding a pale-yellow solid (0.90 g, 67.3%). ^{1}H NMR (500 MHz, $CDCl_3$): δ (ppm) 7.78 (d, 2H), 7.35 (d, 2H), 4.01 (t, 2H), 3.96 (s, 2H), 3.93 (t, 2H), 2.45 (s, 3H), 1.67-1.62 (m, 2H), 1.61-1.56 (m, 2H), 1.38-1.32 (m, 2H), 1.30-1.24 (m, 2H). ^{13}C NMR (125 MHz, $CDCl_3$): δ (ppm) 201.22, 173.85, 144.72, 133.17, 129.86, 127.90, 70.33, 44.46, 35.34, 28.61, 26.45, 26.03, 24.94, 21.67.

2.3.4. 3-(10-(4-Toluenesulfonate)decyl)rhodanine (2b)

Starting from compound 1b (1.20 g, 4.15 mmol), the similar procedure as above afforded compound 2b as a pale-yellow solid (1.18 g, 64.0%). ^{1}H NMR (500 MHz, $CDCl_3$): δ (ppm) 7.79 (d, 2H), 7.35 (d, 2H), 4.01 (t, 2H), 3.96 (s, 2H), 3.96 (t, 2H), 2.45 (s, 3H), 1.64-1.60 (m, 4H), 1.29-1.25 (m, 6H), 1.22-1.21 (m, 6H). ^{13}C NMR (125 MHz, $CDCl_3$): δ (ppm) 201.23, 173.86, 144.73, 133.18, 129.87, 127.91, 70.34, 44.76, 35.41, 32.75, 29.45, 29.36, 29.33, 29.07, 26.71, 26.67, 21.23.

2.3.5. 3-(6-Azidohexyl)rhodanine (3a)

To a mixture of compound 2a (0.90 g, 2.32 mmol) and sodium azide (NaN_3, 1.1 mmol) in anhydrous *N,N*-dimethylformamide (DMF), potassium iodide (KI, 0.1 mmol) was added. The reaction solution was stirred at 50 ℃ for 1 h, and then cooled to room temperature. The reaction solution was extracted with diethyl ether (Et_2O) three times and organic phase was collected, and dried over anhydrous $MgSO_4$. After solvent was evaporated under reduced pressure, the crude product was purified by silica gel column chromatography with CF:EA (19:1 by volume) as eluent, yielding compound 3a as a yellowish viscous liquid (0.43 g, 72.3%). ^{1}H NMR (500 MHz, $CDCl_3$): δ (ppm) 3.98 (t, 2H), 3.97 (s, 2H), 3.26 (t, 2H), 1.69-1.63 (m, 2H), 1.62-1.57 (m, 2H), 1.45-1.34 (m, 4H). ^{13}C NMR (125 MHz, $CDCl_3$): δ (ppm) 201.20, 173.87, 51.32, 44.54, 35.35, 28.67, 26.56, 26.28, 26.24.

2.3.6. 3-(10-Azidodecyl)rhodanine (3b)

By starting from compound 2b (1.18 g, 2.66 mmol), the procedure as above afforded compound 3b as a yellowish viscous liquid (0.47 g, 56.1%). ^{1}H NMR (500 MHz, $CDCl_3$): δ (ppm) 3.97 (t, 2H), 3.96 (s, 2H), 3.26 (t, 2H), 1.66-1.57 (m, 4H), 1.62-1.57 (m, 2H), 1.37-1.25 (m, 12H). ^{13}C NMR (125 MHz, $CDCl_3$): δ (ppm) 201.21, 173.88, 51.51, 44.68, 35.51, 29.45, 29.39, 29.34, 29.31, 29.10, 26.73, 26.68, 26.21.

2.3.7. P3T4Rh-C_6-N_3

To a mixture of P3T4-CHO (300 mg, 0.19 mmol) and compound 3a in 40 mL 1,2-dichloroethane, pyridine (1 mL) and piperidine (0.1 mL) were added. The reaction solution was stirred at 90 ℃ for 18 h and cooled down to room temperature. The reaction solution was extracted with CF three times, and the collected organic phase was dried over anhydrous $MgSO_4$ and concentrated under reduced pressure. The crude compound was purified by silica gel column chromatography with CF as eluent. The eluted solution was concentrated by rotary evaporation and precipitated into MeOH, yielding a dark red solid (285 mg, 73.2%). ^{1}H NMR (500 MHz, $CDCl_3$): δ (ppm) 7.91 (s, 2H), 7.63 (d, 2H), 7.62 (d, 2H), 7.54 (d, 2H), 7.46 (t, 2H), 7.43 (d, 2H). 7.32 (s, 2H), 7.30 (s, 2H), 4.14 (t, 4H), 4.10 (d, 4H), 4.05 (d, 4H), 3.28 (t, 4H), 2.02-1.93 (m, 4H), 1.78-1.72 (m, 4H), 1.68-1.58 (m, 16H), 1.53-1.47 (m, 4H), 1.44-1.37 (m, 24H), 1.35-1.23 (m, 64H), 0.88-0.83 (m, 24H). ^{13}C NMR (125 MHz, $CDCl_3$): δ (ppm) 192.47, 167.68, 156.07, 154.10, 149.89, 148.57 (d, J = 253.08 Hz), 147.56, 139.97, 137.78, 136.27, 134.26, 126.82, 126.68, 126.43, 125.93, 124.21, 121.64, 119.69, 114.99, 111.84, 111.64, 72.49, 51.36, 44.54, 38.30, 31.92, 31.58, 30.07, 29.74, 29.64, 29.37, 28.70, 27.03, 26.98, 26.87, 26.31, 22.70, 14.14, 14.12.

2.3.8. P3T4Rh-C_{10}-N_3

The same procedure with P3T4-CHO (300 mg, 0.19 mmol) and

compound 3b (352 mg, 1.12 mmol) afforded a dark red solid (313 mg, 76.3%). ^{1}H NMR (500 MHz, $CDCl_3$): δ (ppm) 7.93 (s, 2H), 7.63 (d, 2H), 7.62 (d, 2H), 7.54 (d, 2H), 7.45 (t, 2H), 7.44 (s, 2H). 7.33 (s, 2H), 7.30 (s, 2H), 4.12 (t, 4H), 4.10 (d, 4H), 4.05 (d, 4H), 3.26 (t, 4H), 2.00-1.94 (m, 4H), 1.78-1.69 (m, 4H), 1.68-1.58 (m, 16H), 1.53-1.47 (m, 4H), 1.44-1.37 (m, 32H), 1.35-1.23 (m, 72H), 0.88-0.83 (m, 24H). ^{13}C NMR (125 MHz, $CDCl_3$): δ (ppm) 192.46, 167.68, 156.04, 154.07, 149.88, 148.52 (d, J = 264.34 Hz), 139.97, 137.82, 136.26, 134.16, 126.79, 126.66, 126.41, 125.78, 124.17, 121.65, 119.83, 114.89, 111.82, 111.63, 72.49, 51.51, 44.80, 38.32, 38.29, 31.95, 31.93, 31.91, 31.89, 31.64, 31.61, 31.58, 31.55, 30.08, 29.75, 29.64, 29.42, 29.37, 29.33, 29.12, 28.85, 27.05, 27.03, 26.99, 26.77, 26.71, 22.71, 22.70, 14.15, 14.12.

2.3.9. P3T4Rh-Et

To a mixture of P3T4-CHO (300 mg, 0.19 mmol) and 3-ethylrhodanine (180 mg, 1.12 mmol) in 40 mL 1,2-dichloroethane, pyridine (1 mL) and piperidine (0.1 mL) were added. The reaction solution was stirred at 90 ℃ for 14 h and cooled down to room temperature. The reaction solution was extracted with CF three times and the combined organic phase was collected. Organic phase was dried over anhydrous $MgSO_4$ and concentrated under reduced pressure. The crude product was purified by silica gel flash column chromatography with CF:hexane (Hex) (4:1 by volume) as eluent. The purified compound was obtained as s dark red solid (263 mg, 74.5%). ^{1}H NMR (500 MHz, $CDCl_3$): δ (ppm) 7.91 (s, 2H), 7.63 (d, 2H) 7.62 (d, 2H), 7.55 (d, 2H), 7.46 (t, 2H), 7.43 (d, 2H), 7.33 (s, 2H), 7.30 (s, 2H), 4.23 (q, 4H), 4.10 (d, 4H), 4.05 (d, 4H), 2.00-1.94 (m, 4H), 1.67-1.56 (m, 12H), 1.52-1.46 (m, 4H), 1.43-1.36 (m, 16H), 1.34-1.23 (m, 70H), 0.87-0.83 (m, 24H). ^{13}C NMR (125 MHz, $CDCl_3$) δ (ppm) 192.23, 167.45, 149.89, 148.50 (d, J = 266.40 Hz), 137.82, 136.27, 134.16, 126.82, 126.76, 126.67, 126.67, 126.41, 125.78, 124.19, 121.68, 119.92, 111.86, 111.67, 72.51, 39.88, 38.33, 38.30, 31.94, 31.93, 31.91, 31.89, 31.64, 31.61, 31.58, 30.08, 29.74, 29.64, 29.37, 27.05, 27.03, 26.98, 22.71, 22.69, 14.13, 14.11, 12.31. HRMS (MALDI-TOF): $C_{110}H_{158}F_2N_2O_6S_8$, m/z (M^+) = 1897.9812.

2.3.10. [6,6]-Phenyl-C61-butyric acid ($PC_{61}BA$)

To a solution of $PC_{61}BM$ (513 mg, 0.56 mmol) in 50 mL CB, 20 mL acetic acid (AcOH) and 10 mL hydrochloric acid (HCl) were added. The reaction solution was stirred at 120 ℃ for 12 h and cooled down to room temperature. The solvent was removed by vacuum distillation and the remaining solids were dispersed in MeOH and filtered, and washed with MeOH and Et_2O, yielding a black solid as product (460 mg, 91.0%). The dried product was used without further purification.

2.3.11. [6,6]-Phenyl-C61 butyric acid propargyl ester ($PC_{61}BP$)

To a mixture of $PC_{61}BA$ (458 mg, 0.51 mmol), 2-propyn-1-ol (285 mg, 5.1 mmol) and 1-ethyl-3-(3-dimethylaminopropyl)carbodiimide (EDC, 158 mg, 1.02 mmol) in 20 mL *o*-dichlorobenzene (*o*-DCB), 4-dimethylaminopyridine (DMAP, 124 mg, 1.02 mmol) was added. The reaction mixture was stirred at room temperature for 18 h. The reaction mixture was extracted with CF three times and the combined organic phase was dried with anhydrous $MgSO_4$ and concentrated under reduced pressure. The crude product was purified by silica gel column chromatography with CF:Hex (9:1 by volume) as eluent. The product was obtained as a black solid (373 mg, 78.2%). ^{1}H NMR (500 MHz, $CDCl_3$): δ (ppm) 7.93 (dd, 2H), 7.55 (t, 2H), 7.48 (t, 1H), 4.69 (d, 2H), 2.92 (m, 2H), 2.58 (t, 2H), 2.48 (t, 1H), 2.21 (m, 2H). ^{13}C NMR (125 MHz, $CDCl_3$): δ (ppm) 172.21, 148.80, 147.77, 145.86, 145.22, 145.18, 145.09, 145.07, 144.82, 144.80, 144.70, 144.54, 144.47, 144.04, 143.79, 143.16, 143.07, 143.02, 142.96, 142.27, 142.20, 142.16, 142.14, 141.04, 140.78, 138.09, 137.60, 136.70, 132.12, 128.49, 128.30, 79.84, 77.64, 75.02, 52.05, 51.79, 33.80, 33.63, 22.24.

2.3.12. P3T4Rh-C_6-$PC_{61}BM$

To a mixture of P3T4-C_6-N_3 (200 mg, 0.10 mmol), $PC_{61}BP$ (0.21 mmol), and CuBr (10 mg) in 25 mL freshly-degassed toluene, 0.1 mL of *N,N,N′,N″,N″*-pentamethyldiethylenetriamine (PMDETA) was added dropwise in dark condition. The reaction mixture was stirred at room temperature for 2 h. The reaction mixture was passed through the celite pad to remove the catalyst and the solvent was removed in vacuum. The crude compound was purified by silica gel column chromatography with CF:MeOH (25:1 by volume) as eluent. The collected solid was filtered and washed with MeOH, Hex, and EA sequentially, yielding a dark black solid (285 mg, 75.3%). ^{1}H NMR (500 MHz, $CDCl_3$): δ (ppm) 7.92-7.90 (m, 6H), 7.62 (t, 4H), 7.58 (s, 2H), 7.55-7.52 (m, 6H), 7.48-7.45 (m 4H), 7.43 (d, 2H), 7.32 (s, 2H), 7.29 (s, 2H), 5.23 (s, 4H), 4.34 (t, 4H), 4.11 (t, 4H), 4.08 (d, 4H), 4.03 (d, 4H), 2.89 (m 4H), 2.55 (t, 4H), 2.18 (m, 4H), 2.00-1.91 (m, 8H), 1.73 (m, 4H) 1.64-1.57 (m, 12H), 1.51-1.46 (m, 4H), 1.43-1.37 (m, 24H), 1.33-1.19 (m, 64H), 0.87-0.83 (m, 24H). ^{13}C NMR (125 MHz, $CDCl_3$): δ (ppm) 192.45, 172.96, 167.65, 149.92, 149.61, 149.36, 148.78, 146.78 (d, J = 244.68 Hz), 145.17, 145.04, 144.78, 144.65, 144.49, 144.00, 143.74, 142.99, 142.80, 142.19, 140.98, 140.75, 139.99, 138.03, 137.76, 137.57, 136.72, 134.80, 134.38, 132.11, 128.47, 128.27, 126.83, 126.51, 126.09, 124.30, 123.55, 119.58, 111.90, 111.67, 79.85, 72.48, 57.84, 51.80, 50.31, 44.35, 38.36, 33.92, 33.63, 31.94, 31.60, 30.10, 29.77, 29.66, 29.39, 27.07, 27.00, 26.72, 26.08, 22.72, 22.25, 14.16. HRMS (MALDI-TOF): $C_{266}H_{200}F_2N_8O_{10}S_8$, m/z ($M+Na^+$) = 3985.6154.

2.3.13. P3T4Rh-C_{10}-$PC_{61}BM$

Starting from P3T4Rh-C_{10}-N_3 (200 mg, 0.10 mmol), the similar procedure as above afforded the product as a dark black solid (298 mg, 80.7%). ^{1}H NMR (500 MHz, $CDCl_3$): δ (ppm) 7.92-7.89 (m, 6H), 7.63 (d, 2H), 7.61 (d, 2H) 7.57 (s, 2H), 7.55-7.52 (m, 6H), 7.48-7.45 (m 4H), 7.42 (d, 2H), 7.32 (s, 2H), 7.29 (s, 2H), 5.22 (s, 4H), 4.33 (t, 4H), 4.13-4.06 (m, 8H), 4.04 (d, 4H), 2.89 (m 4H), 2.54 (t, 4H), 2.18 (m, 4H), 2.00-1.94 (m, 4H), 1.89 (m, 4H), 1.73 (m, 4H) 1.65-1.55 (m, 20H), 1.51-1.46 (m, 4H), 1.43-1.37 (m, 16H), 1.33-1.19 (m, 88H), 0.87-0.83.(m, 24H). ^{13}C NMR (125 MHz, $CDCl_3$): δ (ppm) 192.45, 172.95, 167.66, 154.10, 149.90, 149.59, 148.78, 147.54, 146.81 (d, J = 243.81 Hz), 145.19, 145.15, 145.06, 145.04, 144.78, 144.75, 144.68, 144.65, 144.50, 144.42, 144.01, 143.75, 143.12, 143.04, 142.99, 142.93, 142.91, 142.71, 142.20, 142.17, 142.12, 142.09, 140.99, 140.76, 139.99, 138.03, 137.82, 137.58, 136.72, 136.27, 134.23, 132.10, 128.46, 128.27, 126.81, 126.71, 126.47, 125.85, 124.22, 123.54, 121.68, 121.67, 119.81, 111.89,

111.67, 79.85, 72.49, 57.82, 51.81, 50.45, 44.77, 38.35, 38.31, 33.93, 33.64, 31.96, 31.93, 31.90, 31.66, 31.63, 31.61, 31.59, 31.57, 30.28, 30.10, 29.76, 29.65, 29.38, 29.25, 29.07, 28.93, 27.06, 26.99, 26.72, 26.47, 22.71, 22.26, 14.17, 14.14. HRMS (MALDI-TOF): $C_{274}H_{216}F_2N_8O_{10}S_8$, *m/z* ($M+Na^+$) = 4096.8719.

3. Results and discussion

3.1. Synthesis of P3T4Rh-C_n-$PC_{61}BM$ SC triads

Scheme 1 shows the synthetic procedure for the A-D-A-type SC triads of P3T4Rh-C_n-$PC_{61}BM$ (n = 6, 10). The P3T4 core was used as an electron-donating core; it is reportedly a highly crystalline building block owing to the intrachain noncovalent coulombic interactions of C-$H^{\delta+}\cdots F^{\delta-}$ and $S^{\delta+}\cdots O^{\delta-}$, which yield a planar conformation through the molecular backbone.[37-41] The planar conjugated P3T4 building blocks are expected to cause strong cofacial π-π interaction between the molecules, resulting in crystalline intermolecular packing with efficient carrier transport in a vertical direction in the film. $PC_{61}BM$ was incorporated as an electron-accepting moiety at both termini. In addition, the alkyl spacer length (n = 6 or 10) was also modulated because the terminal bulky $PC_{61}BM$ hinders the intermolecular packing interaction, where the steric hindrance can be mitigated by controlling the spacer length between the P3T4 core and terminal $PC_{61}BM$.

To synthesize azide (N_3)-functionalized rhodanine (Rh) moieties, the hydroxyalkyl-substituted Rh structures (**1a**: n = 6, **1b**: n = 10) were first synthesized in 20%-25% yield using a microwave-assisted one-pot reaction between amino alcohols (6-amino-1-hexanol or 10-amino-1-decanol) and bis(carboxymethyl)trithiocarbonate. A subsequent tosylation reaction using 4-toluenesulfonyl chloride yielded compounds **2a** and **2b** in 64%-67% yield. Finally, **3a** (**3b**) was synthesized in 72% (56%) yield by reacting compound **2a** (**2b**) with NaN_3 in the presence of a catalytic amount of KI in DMF. To prepare P3T4Rh-C_n-N_3, P3T4-CHO was first prepared by following previously reported synthetic procedures.[37] Knoevenagel condensation reaction between P3T4-CHO and the azide-functionalized **3a** (**3b**) produced P3T4Rh-C_6-N_3 (P3T4Rh-C_{10}-N_3) in ~70% yield. To synthesize alkyne-functionalized $PC_{61}BP$, $PC_{61}BM$ was first hydrolyzed to produce $PC_{61}BA$ using AcOH and HCl in CB (91% yield). Then, $PC_{61}BP$ was successfully synthesized in 78.2% yield *via* Steglich esterification with $PC_{61}BA$ and propargyl alcohol in the presence of EDC and DMAP in *o*-DCB.

To couple P3T4Rh-C_n-N_3 and $PC_{61}BP$, click chemistry was adopted using copper (I)-catalyzed azide-alkyne 1,3-dipolar cycloaddition to form a cyclic 1,2,3-triazole linkage.[42-44] The click coupling reaction was conducted under strictly anaerobic conditions using CuBr and PMDETA to yield the target A-D-A triads, P3T4Rh-C_6-$PC_{61}BM$ and P3T4Rh-C_{10}-$PC_{61}BM$, in 75% and 80% yields, respectively.[44] The polar 1,2,3-triazole moieties in the final structures modulate the polarity of P3T4Rh-C_6-$PC_{61}BM$ and P3T4Rh-C_{10}-$PC_{61}BM$ against that of other byproducts, which enables easy purification by silica gel column chromatography.

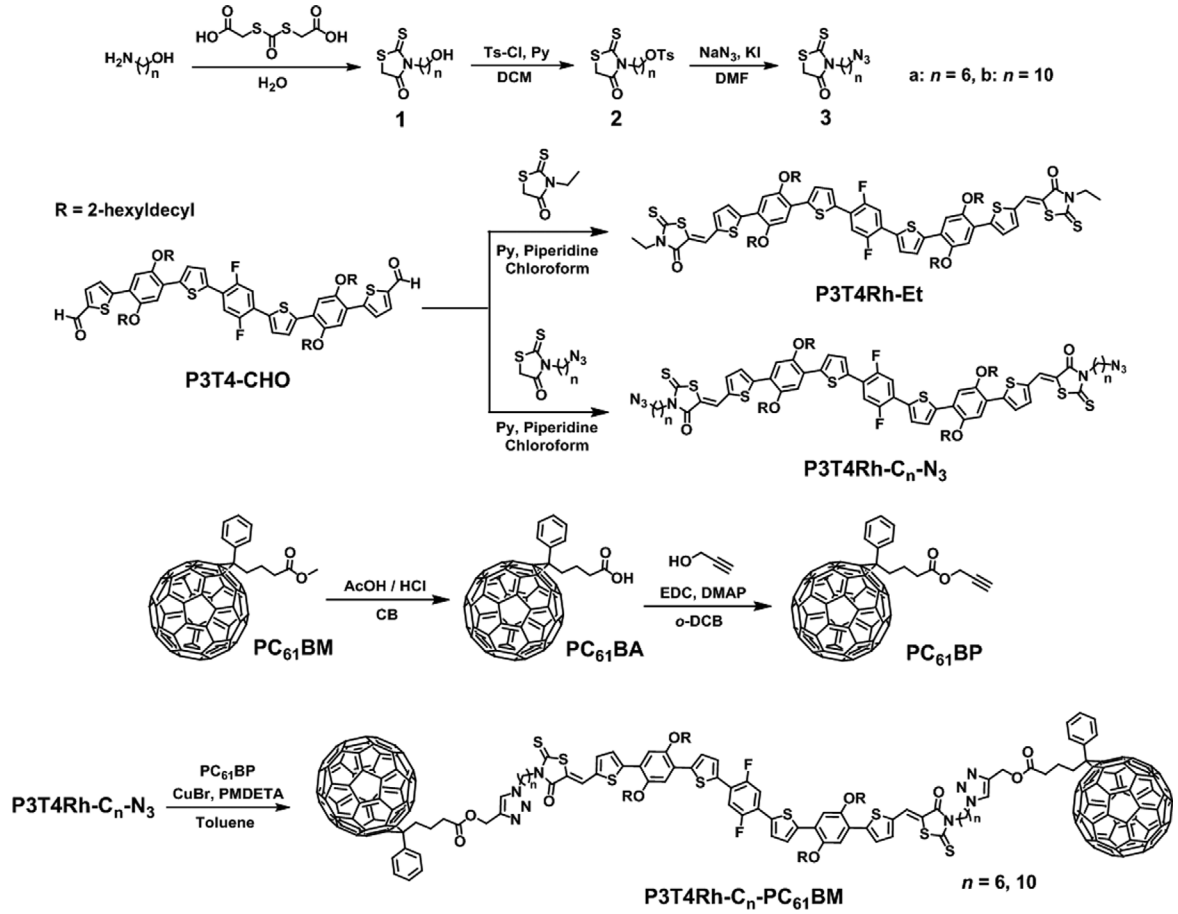

Scheme 1. Synthetic scheme of P3T4Rh-C_n-$PC_{61}BM$ SC photoactive molecules.

The Rh-substituted core itself, P3T4Rh-Et, was also synthesized in 75% yield by Knoevenagel condensation between P3T4-CHO and 3-ethylrhodanine as a reference material. All the intermediates and final triad structures were characterized by ^{1}H and ^{13}C NMR spectroscopy and HRMS spectroscopy using MALDI-TOF mass spectrometry, which confirmed the suggested molecular structures.

3.2. Thermal, optical, and electrochemical properties

TGA and DSC were performed to examine the thermal properties of the materials (Figure S1). As shown in the TGA thermograms, the decomposition temperatures (T_d, 5% weigh loss) of P3T4Rh-Et, P3T4Rh-C_6-$PC_{61}BM$, and P3T4Rh-C_{10}-$PC_{61}BM$ were found to be 364.5 ℃, 360.3 ℃, and 357.5 ℃, respectively. As the decomposition of the ester linkage in $PC_{61}BM$ typically occurs above 380 ℃ in previous studies,[31,45] the thermal decomposition at a lower temperature of approximately 360 ℃ in the P3T4 SC series is interpreted as indicating the breakup of the triazole linkage between the P3T4 core and $PC_{61}BM$.[41,42] In the DSC thermograms, a melting temperature (T_m) of 160 ℃ and recrystallization temperature (T_c) of 126 ℃ were clearly observed for P3T4Rh-Et. However, no discernable thermal transitions were observed at 25-270 ℃ for the SC molecules, indicating their amorphous nature. The incorporation of bulky terminal $PC_{61}BM$ may significantly disrupt the intermolecular crystalline packing of the P3T4 cores.

Figure 1(a) shows the UV-vis spectra of P3T4Rh-Et, $PC_{61}BM$, P3T4Rh-C_6-$PC_{61}BM$, and P3T4Rh-C_{10}-$PC_{61}BM$ in CF and in film. In solution, P3T4Rh-Et shows maximum absorption at λ_{abs}= 507.5 nm, and two SC molecules also had similar spectra with λ_{abs}=507-510 nm because all the structures had the same core. As shown in Figure 1(a), P3T4Rh-Et and $PC_{61}BM$ have complementary absorption in the UV-vis region, and the absorption spectra of the SC molecules combine the features of these two compounds. Two P3T4Rh-C_6-$PC_{61}BM$ and P3T4Rh-C_{10}-$PC_{61}BM$ molecules are linked by σ-alkyl chain linkers, and the core and terminal $PC_{61}BM$ groups are not conjugated. Similar molar absorption coefficient of the P3T4Rh core (at λ_{abs}=510 nm) was measured for P3T4Rh-Et (1.24×10^5 $M^{-1}\cdot cm^{-1}$), P3T4Rh-C_6-$PC_{61}BM$ (1.29×10^5 $M^{-1}\cdot cm^{-1}$) and P3T4Rh-C_{10}-$PC_{61}BM$ (1.27×10^5 $M^{-1}\cdot cm^{-1}$) in CF, because of no electronic conjugation between the core and $PC_{61}BM$ terminal moieties. The spectrum of the P3T4Rh-Et film was significantly red-shifted, with λ_{abs}=574.5 nm, because of enhanced π-π stacking interaction in the solid state. A pronounced 0-0 transition was clearly observed, suggesting tight intermolecular packing of the planar P3T4 cores. In contrast to P3T4Rh-Et, both SC triad structures show UV-vis spectra with λ_{abs}=528-530 nm in film, with much smaller red shifts compared to those in solution, indicating that the π-π interaction between the P3T4 cores in the SC triads is significantly hindered compared to that in P3T4Rh-Et. In addition, the substantially smaller absorption coefficient of P3T4Rh-C_6-$PC_{61}BM$ (1.09×10^5 cm^{-1} at λ_{abs}=528 nm) and P3T4Rh-C_{10}-$PC_{61}BM$ (1.06×10^5 cm^{-1} at λ_{abs}=530 nm) in film was measured compared to that of P3T4Rh-Et (1.60×10^5 cm^{-1} at λ_{abs}=574.5 nm) at the λ_{abs} of the P3T4 core, suggesting that the significantly reduced intermolecular packing interaction of P3T4 cores in SC materials (Table S1). P3T4Rh-Et and P3T4Rh-C_n-$PC_{61}BM$ SC are expected to have significantly different packing characteristics, which are discussed in detail in the following section. To adjust the packing properties of the P3T4 core in the SC systems, thermal annealing (TA) and SVA were applied to the films, and the corresponding UV-vis absorption spectra were further investigated (Figure S2). A TA temperature of 145 ℃ was chosen on the basis of DSC measurements of P3T4Rh-Et between its T_c and T_m values. As a result of TA, the

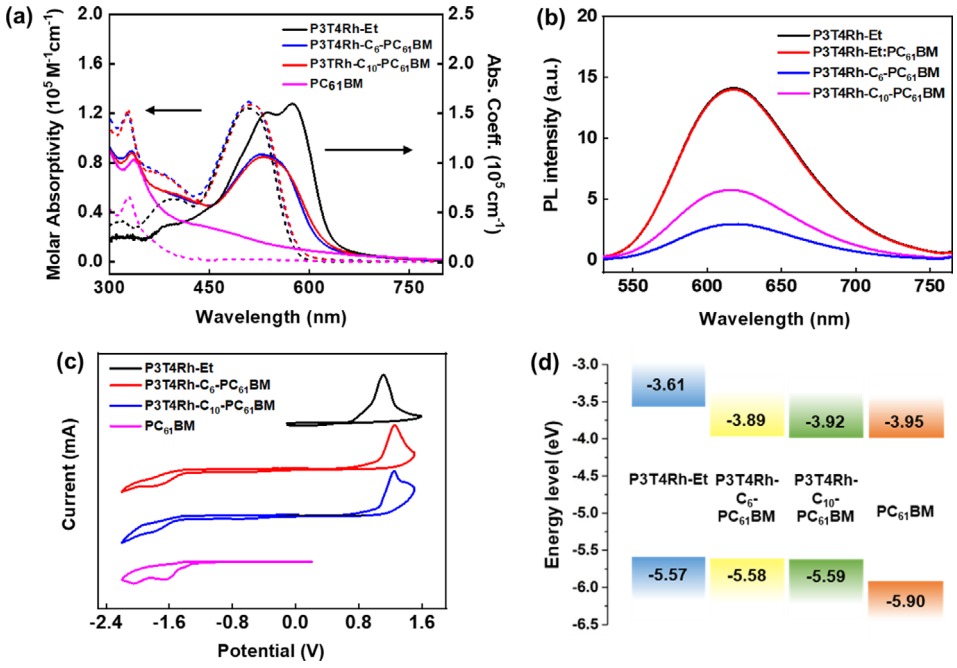

Figure 1. (a) Absorption coefficients in CF (dashed) and in film (solid), (b) PL spectra in CF (λ_{ex}=510 nm), (c) cyclic voltammograms, and (d) FMO energy level diagram of P3T4Rh-C_n-$PC_{61}BM$ SC triads.

spectra of P3T4Rh-Et showed a dramatic change, with an intensified 0-0 transition and well-resolved vibronic structures, whereas the spectra of the SC triads showed negligible changes. SVA is also an effective method of improving the crystalline packing of solution-processed organic semiconductor films.[46] SVA was conducted for 90 s by placing the films in a chamber (5×5 cm^2) containing 5 mL of EA. SVA of the P3T4Rh-Et and SC triad films yielded results similar to those of TA. P3T4Rh-Et showed significant changes, with a more intense π-π stacking peak in the UV-vis spectrum, but no recognizable changes were observed for the P3T4Rh-C_6-PC_{61}BM and P3T4Rh-C_{10}-PC_{61}BM films. The packing characteristics of P3T4Rh-Et were very sensitive to external stimulation such as TA and SVA post-treatments and exhibited improved intermolecular stacking because of the conformational locking of the planar P3T4 structure *via* noncovalent coulombic interactions along the conjugated backbone. However, in the A-D-A-type SC triads, the ordered (or packed) P3T4 structures were poorly constructed regardless of post-treatment due to the bulky terminal PC_{61}BM moieties, even with increased spacer length in P3T4Rh-C_{10}-PC_{61}BM. From the absorption onset in the films, the optical band gap (E_g^{opt}) was determined to be 1.96 eV for P3T4Rh-Et, 2 eV for P3T4Rh-C_6-PC_{61}BM, and 1.98 eV for P3T4Rh-C_{10}-PC_{61}BM.

To investigate the intramolecular charge transfer (ICT) interaction in the SC systems, steady-state photoluminescence (PL) experiments were conducted in extremely diluted solution (~3.5×10^{-7} M) in CF under excitation at λ_{ex}=510 nm (Figure 1(b)). The PL intensity of the P3T4Rh-Et/PC_{61}BM (1:2 M ratio) blend solution is similar to that of P3T4Rh-Et, indicating negligible PL quenching. In the diluted solution, the intermolecular charge transfer is negligible because of the large separation between the p- and n-type moieties (P3T4Rh-Et and PC_{61}BM) in the blend solution. However, both SC triads show significant PL quenching under the same conditions. The PL quenching efficiency was determined to be 78.8% for P3T4Rh-C_6-PC_{61}BM and 59.6% for P3T4Rh-C_{10}-PC_{61}BM. The more efficient PL quenching in P3T4Rh-C_6-PC_{61}BM can be understood in terms of the shorter D-A spacing and thus more efficient ICT. The significant PL quenching in both SC triad structures is strong evidence of efficient intramolecular exciton separation by photoinduced electron transfer from the p-type core to the terminal fullerenes, which might offer an additional charge transfer pathway for exciton separation in these SC photovoltaic systems, in contrast to the D/A blended systems.

The cyclic voltammograms of P3T4Rh-Et, PC_{61}BM, P3T4Rh-C_6-PC_{61}BM, and P3T4Rh-C_{10}-PC_{61}BM were measured in thin film (coated on a platinum working electrode) in a 0.1 M Bu_4NBF_4 acetonitrile solution (Figure 1(c)). A platinum wire and $Ag/AgNO_3$ were used as the counter electrode and reference electrode, respectively. The estimated frontier molecular orbital (FMO) levels relative to the internal standard of the ferrocene/ferrocenium (Fc/Fc^+) redox couple are shown in Figure 1(d). P3T4Rh-Et and PC_{61}BM showed highest occupied molecular orbital (HOMO)/lowest unoccupied molecular orbital (LUMO) energy levels of -5.57/-3.61 eV and -5.90/-3.95 eV, respectively. The HOMO/LUMO energy levels of the SC molecular systems were determined to be -5.58/-3.89 eV and -5.59/-3.92 eV for P3T4Rh-C_6-PC_{61}BM and P3T4Rh-C_{10}-PC_{61}BM, respectively. In both structures, the oxidation and reduction peaks originate from the P3T4Rh and PC_{61}BM moieties, which determine the HOMO and LUMO levels in the SC systems. The FMO energy levels confirm that there is sufficient energy offset for both electron and hole transfer between the two moieties. In addition, the spacer length had no effect on the oxidation and reduction potentials of the two SC structures, because there was no conjugation between the p- and n-type blocks. The optical, electrical, and thermal properties are summarized in Table 1.

3.3. Morphological properties

The film morphologies of P3T4Rh-Et and the two SC triads were investigated by GIWAXS and AFM measurements. Two-dimensional GIWAXS images and line cuts are shown in Figure 2 and corresponding packing parameters are summarized in Table S2. P3T4Rh-Et shows lamellar scatterings (*d*-spacing of 21.3 Å) up to (400) along the out-of-plane (OOP) direction. The in-plane (IP) (100) lamellar peak was also observed together with a π-π stacking (010) signal (*d*-spacing of 3.8 Å) along the OOP direction. The GIWAXS analysis indicates that P3T4Rh-Et has preferential edge-on packing with a mixed bimodal orientation (Figure 2(a)). Overall, the pronounced crystalline packing of P3T4Rh-Et originates from its planar p-conjugated backbone and is based on the design motif of intramolecular noncovalent coulombic interactions along the backbone. By contrast, the corresponding lamellar and π-π stacking peaks of the P3T4 core almost disappeared in the images of both the P3T4Rh-C_6-PC_{61}BM and P3T4Rh-C_{10}-PC_{61}BM films (Figure 2(b) and 2(c), respectively), indicating their amorphous morphology. The broad peak at q=1.39 $Å^{-1}$ is ascribed to aggregated PC_{61}BM molecules. The surface roughness was studied by AFM, and Figure S3 shows topographic images of the P3T4Rh-C_6-PC_{61}BM and P3T4Rh-C_{10}-PC_{61}BM films. Both films show very smooth surfaces with root-mean-square

Table 1. Summary of optical, electrochemical, and thermal properties

Material	λ_{abs} (soln) (nm)	λ_{abs} (film) (nm)	λ_{onset} (film) (nm)	E_g^{opt} (eV)[a]	HOMO (eV)[b]	LUMO (eV)	T_d (°C)[e]
P3T4Rh-Et	507.5	574.5	632.2	1.96	−5.57	−3.61[c]	364.5
P3T4Rh-C_6-PC_{61}BM	510.3	528.0	619.5	2.00	−5.58	−3.89[d]	360.3
P3T4Rh-C_{10}-PC_{61}BM	507.7	530.0	626.5	1.98	−5.59	−3.92[d]	357.5

[a] E_g^{opt} was estimated from the absorption onset in film. [b]HOMO level was estimated from the tangential onset of oxidation (E_{ox}^{onset}) observed by cyclic voltammetry. [c]LUMO level was estimated from the HOMO value and E_g^{opt} in film. [d]LUMO level was estimated from the tangential onset of the reduction peak (E_{red}^{onset}). [e]T_d (5% weight loss) was determined by TGA under nitrogen.

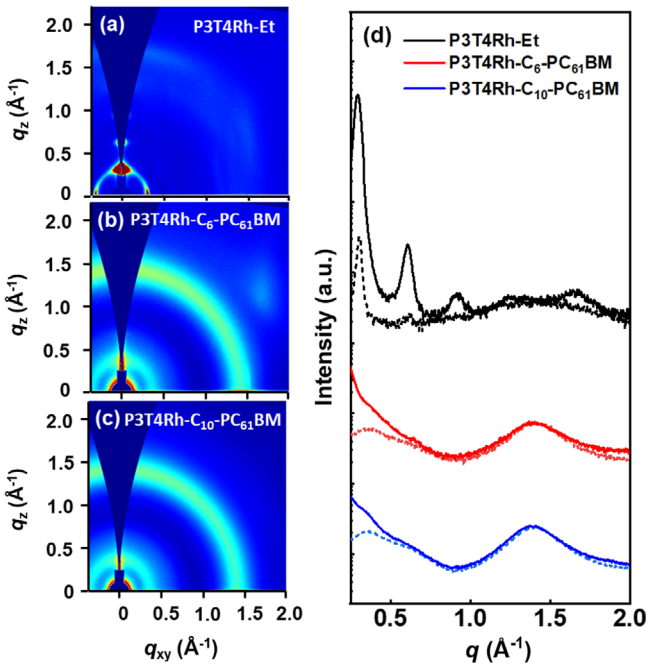

Figure 2. GIWAXS images of (a) P3T4Rh-Et, (b) P3T4Rh-C_6-$PC_{61}BM$, and (c) P3T4Rh-C_{10}-$PC_{61}BM$ films. (d) Corresponding line cuts along the IP (dashed) and OOP (solid) directions.

roughness values of 0.31 and 0.30 nm for P3T4Rh-C_6-$PC_{61}BM$ and P3T4Rh-C_{10}-$PC_{61}BM$ films, respectively. The smooth surfaces of these films are expected to be related to their amorphous morphology, which is consistent with the UV-vis spectra, DSC measurements, and GIWAXS analysis.

3.4. Photovoltaic properties

The photovoltaic properties of the P3T4-based SC triads were investigated to test their diode characteristics by fabricating SCOSC devices with a conventional architecture of ITO/PEDOT:PSS/active layer/ZnO/Al. The SCOSC devices were tested by varying the processing solvent, solution concentration, additives, etc. The optimized devices were fabricated using a total SC material concentration of 20 mg/mL in CB with 1 vol.% DPE as a processing additive. The *J-V* characteristics of the optimized devices are shown in Figure 3, and the detailed photovoltaic parameters are summarized in Table 2. The optimized P3T4Rh-C_6-$PC_{61}BM$ and P3T4Rh-C_{10}-$PC_{61}BM$ devices showed similar PCEs of 0.43% and 0.40%, with J_{SC} values of 1.92 and 1.83 mA cm^{-2} and open-circuit voltage (V_{OC}) values of 0.85 and 0.82 V, respectively; the FF value of both devices was 0.27. Overall, the photovoltaic characteristics of the P3T4-based SC triads are significantly lower than those (PCE: 2.44%, J_{SC}: 7.02 mA cm^{-2}, V_{OC}: 0.97 V, FF: 0.36) of previously reported BDTRh-PCBM SCOSCs based on the BDT core.[31] P3T4Rh-C_6-$PC_{61}BM$ and BDTRh-PCBM are A-D-A-type SC triads with similar structure that contain $PC_{61}BM$ as an electron-withdrawing moiety at both termini. The different donor moieties in the SC triads resulted in significantly different photoelectrical properties, emphasizing the importance of careful choice of the donor moiety in the design of fullerene-based SC photovoltaic structures.

To understand the poor photoelectrical properties of the P3T4-based SCOSCs, we further investigated the charge mobility using the space-charge-limited current method. The hole and electron mobilities in the vertical direction were measured by fabricating hole-only and electron-only devices with a device structure of ITO/PEDOT:PSS/active layer/Au and ITO/ZnO/active layer/Al, respectively. The measured hole (μ_h) and electron (μ_e) mobilities of the P3T4Rh-C_6-$PC_{61}BM$ and P3T4Rh-C_{10}-$PC_{61}BM$ films are μ_h=3.62×10^{-6}/μ_e=9.67×10^{-7} cm^2 $V^{-1}s^{-1}$ and μ_h=3.23×10^{-6}/μ_e=3.82×10^{-7} cm^2 $V^{-1}s^{-1}$, respectively. Both devices show unbalanced hole and electron mobilities, which is one of the reasons for the low FF of devices. Because the charge carrier extraction is limited by the carrier with lower mobility, the imbalanced carrier transport increases current losses from charge recombination, resulting in low FF of photovoltaic devices.[47,48] The μ_e value of P3T4Rh-C_6-$PC_{61}BM$ is 2.5 times higher, which may

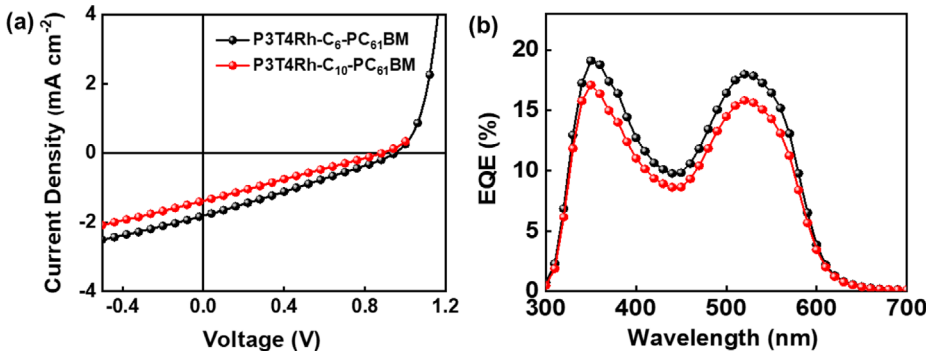

Figure 3. (a) *J-V* characteristics and (b) EQE spectra of optimized P3T4Rh-C_6-$PC_{61}BM$- and P3T4Rh-C_{10}-$PC_{61}BM$-based SCOSCs.

Table 2. Photovoltaic parameters of P3T4Rh-C_6-$PC_{61}BM$- and P3T4Rh-C_{10}-$PC_{61}BM$-based SCOSCs

Active material	V_{OC} (V)	J_{SC} (mA cm^{-2})	FF	PCE[a] (%)
P3T4Rh-C_6-$PC_{61}BM$	0.85 (0.82±0.03)	1.92 (1.82±0.10)	0.27 (0.27±0.02)	0.43 (0.42±0.01)
P3T4Rh-C_{10}-$PC_{61}BM$	0.82 (0.80±0.02)	1.83 (1.72±0.09)	0.27 (0.27±0.02)	0.40 (0.38±0.02)

[a]Average photovoltaic parameters and standard deviations are based on measurements of 10 independent devices.

explain its higher J_{SC} compared to that of P3T4Rh-C_{10}-PC_{61}BM. Because of the flexible spacer length, we expected that the longer (C10) spacer might improve the intermolecular packing of the P3T4 cores in P3T4Rh-C_{10}-PC_{61}BM with reduced steric crowdedness. However, the effect of alkyl spacer length on the packing structure was negligible, and both P3T4Rh-C_6-PC_{61}BM and P3T4Rh-C_{10}-PC_{61}BM showed amorphous morphology. Thus, the longer decyl spacer in P3T4Rh-C_{10}-PC_{61}BM may further increase the insulating property by hindering electron transport in the active layer. In addition, the carrier mobilities are significantly lower than those (μ_h=1.03×10^{-6} cm^2 V^{-1} s^{-1} and μ_e=8.96×10^{-6} cm^2 V^{-1} s^{-1}) of BDTRh-PCBM, indicating critical dependence on the conjugated core in A-D-A-type SC triad structures.[31]

The *J-V* characteristics of P3T4Rh-C_6-PC_{61}BM and P3T4Rh-C_{10}-PC_{61}BM were further investigated under dark conditions (Figure 4(a)), and the leakage current and rectification ratio were measured to evaluate the diode properties. Both SCOSC devices showed a very high leakage current (~5 mA cm^{-2}) and low rectification ratio (~20), indicating very poor diode behavior of both SC structures, which is attributed to their amorphous morphology in film. The photocurrent density (J_{ph}) versus effective voltage (V_{eff}) characteristics of the two SCOSCs were also investigated (Figure 4(b)). J_{ph} is defined as $J_{ph}=J_L-J_D$, where J_L and J_D are the photocurrent densities under illumination and in the dark, respectively. V_{eff} is defined as $V_{eff}=V_0-V_a$, where V_0 is the voltage at which J_{ph} is zero, and V_a is the applied bias voltage. We did not observe saturation of J_{ph} even at high V_{eff} (>2 V) in either the P3T4Rh-C_6-PC_{61}BM or P3T4Rh-C_{10}-PC_{61}BM device, probably because of severe trap-assisted charge recombination originating from the amorphous film morphology. The high leakage current and charge recombination in the P3T4-based SCOSCs also caused a significant decrease in V_{OC}, which is related to the energy difference between the HOMO of the donor and LUMO of the acceptor. The HOMO of P3T4Rh-C_6-PC_{61}BM and P3T4Rh-C_{10}-PC_{61}BM was determined to be approximately -5.6 eV, which is significantly deeper than that (-5.32 eV) of BDTRh-PCBM based on a BDT core. However, the measured V_{OC} values (0.82-0.85 V) were significantly lower than that of BDTRh-PCBM (0.97 V).[31] V_{OC} is defined as follows:

$$V_{OC} = nk_BT/q \ln(J_{ph}(V_{OC})/J_0+1) \quad (1)$$

where n, k_B, T, and q are the ideality factor of the diode, Boltzmann's constant, the temperature (K), and the elementary charge, respectively.[49,50] V_{OC} depends on the variables $J_{ph}(V_{OC})$ and J_0, which are the photocurrent at V_{OC} and the leakage current, respectively. Therefore, the significant decrease in V_{OC} in the P3T4-based SCOSCs can be interpreted in terms of the low $J_{ph}(V_{OC})$ and high leakage current, in good agreement with the measured *J-V* characteristics.

The light intensity (P_{light})-dependent J_{SC} and V_{OC} characteristics were also measured to investigate the charge carrier recombination properties (Figure 4(c) and 4(d)).[49,51] The P_{light} versus J_{SC} curves were fitted according to a power-law equation, $J_{SC} \propto I^{\alpha}$ (where I is the light intensity, and α is the slope of a logarithmic plot of J_{SC} versus light intensity). The slopes of log-log plots of P_{light} versus J_{SC} were found to be 0.91 and 0.92 for the P3T4Rh-C_6-PC_{61}BM and P3T4Rh-C_{10}-PC_{61}BM SCOSCs, respectively. Negligible bimolecular recombination is expected at α=1. The low α values of ~0.9 indicate that both SCOSC devices suffer from serious bimolec-

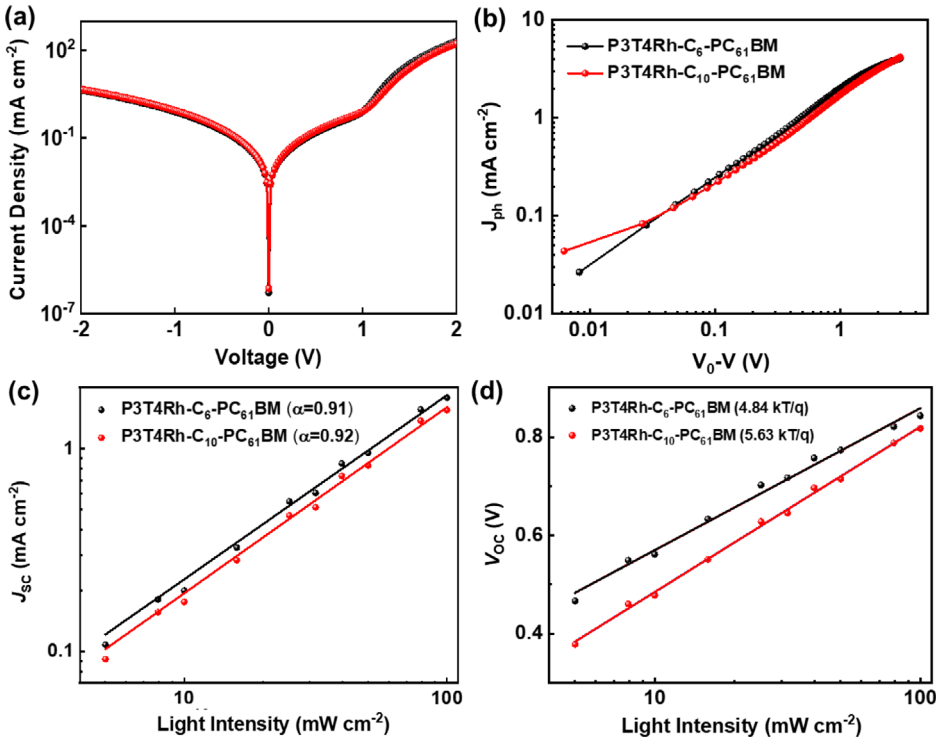

Figure 4. (a) *J-V* characteristics of P3T4Rh-C_6-PC_{61}BM and P3T4Rh-C_{10}-PC_{61}BM in the dark, (b) photocurrent density (J_{ph}) versus effective voltage (V_{eff}) characteristics, and dependence of (c) J_{SC} and (d) V_{OC} on light intensity.

ular recombination. The P_{light} versus V_{OC} curves were fitted according to the equation $V_{OC} \propto nkT/q \ln(P_{light})$. When the ideality factor is unity, the carrier recombination in the depletion region is negligible, and the diffusion current is dominant in the device. By contrast, a value of n=2 indicates that trap-assisted recombination is dominant. Typical devices exhibit both recombination and diffusion currents; thus, the value of n is often measured in the range of 1 to 2. As shown in the semilogarithmic plots of P_{light} versus V_{OC}, both the P3T4Rh-C_6-PC_{61}BM and P3T4Rh-C_{10}-PC_{61}BM devices have unusually high n values (4.84 and 5.63, respectively), again confirming the poor diode characteristics, which must be strongly related to the amorphous film morphology. A comparison of the morphological and photovoltaic properties of BDTRh-PCBM indicates that the polyaromatic fused core is a better choice than the single-bond-based conformation-locked conjugated core in the design of A-D-A-type SC triads to induce crystalline packing and enhanced photoelectrical properties.[31]

4. Conclusions

Two A-D-A-type SC photoactive triads (P3T4Rh-C_6-PC_{61}BM and P3T4Rh-C_{10}-PC_{61}BM) were synthesized on the basis of a P3T4 core, which was designed to have a planar conformation *via* noncovalent coulombic interactions along the main conjugated backbone. A fullerene derivative (PC_{61}BM) was incorporated at each terminus, and the spacer length was varied (C6 and C10) to modulate the intermolecular packing interactions of SC molecules. In dilute solution, both SC triads showed clear PL quenching by ICT, which may offer an additional exciton separation pathway in SCOSCs compared to D/A blended devices. The donor moiety, P3T4Rh-Et, showed strong intermolecular packing with pronounced lamellar scatterings up to (400) along the OOP direction in GIWAXS measurements. However, the ordered structure of the P3T4 cores was almost completely destroyed by the incorporation of the bulky PC_{61}BM terminal moieties, indicating that both SC triads had amorphous morphology. The morphological changes were in good agreement with the UV-vis spectra, *J-V* characteristics, carrier mobility, and light-intensity-dependent J_{SC} and V_{OC} characteristics of the SC triads. Because of poor carrier transport (with severe bimolecular and trap-assisted recombination) and poor diode characteristics, the obtained SCOSCs based on P3T4Rh-C_6-PC_{61}BM and P3T4Rh-C_{10}-PC_{61}BM showed significantly lower PCEs (~0.4%) than previously reported BDTRh-PCBM SCOSCs based on a fused donor core (2.44%).[31] This study suggested that a polyaromatic fused core could be considered a better choice for the design of A-D-A-type SC triads than a single-bond-based conjugated core with conformational locking, as it is better able to induce crystalline packing and thus enhance the photoelectrical properties of SC photoactive molecules.

Supporting information: Supporting information is available including followings: experimental results for TGA, DSC thermograms, AFM topographic images, GIWAXS packing parameters, and NMR spectra. The materials are available *via* the Internet at http://www.springer.com/13233.

References

(1) K. Fukuda, K. Yu, and T. Someya, *Adv. Energy. Mater.*, **10**, 2000765 (2020).
(2) D. Koo, S. Jung, J. Seo, G. Jeong, Y. Choi, J. Lee, S.M. Lee, Y. Cho, M. Jeong, J. Lee, J. Oh, C. Yang, and H. Park, *Joule*, **4**, 1021 (2020).
(3) G. D. Wang, M. A. Adil, J. Q. Zhang, and Z. X. Wei, *Adv. Mater.*, **31**, 1805089 (2019).
(4) M. Kaltenbrunner, M. S. White, E. D. Glowacki, T. Sekitani, T. Someya, N. S. Sariciftci, and S. Bauer, *Nat. Commun.*, **3**, 770 (2012).
(5) C. Li, J. D. Zhou, J. L. Song, J. Q. Xu, H. T. Zhang, X. N. Zhang, J. Guo, L. Zhu, D. H. Wei, G. C. Han, J. Min, Y. Zhang, Z. Q. Xie, Y. P. Yi, H. Yan, F. Gao, F. Liu, and Y. M. Sun, *Nat. Energy.*, **6**, 605 (2021).
(6) C. Zhu, L. Meng, J. Y. Zhang, S. C. Qin, W. B. Lai, B. B. Qiu, J. Yuan, Y. Wan, W. C. Huang, and Y. F. Li, *Adv. Mater.*, **33**, 2100474 (2021).
(7) Y. Cui, H. F. Yao, J. Q. Zhang, K. H. Xian, T. Zhang, L. Hong, Y. M. Wang, Y. Xu, K. Q. Ma, C. B. An, C. He, Z. X. Wei, F. Gao, and J. H. Hou, *Adv. Mater.*, **32**, 1908205 (2020).
(8) G. Y. Zhang, H. J. Ning, H. Chen, Q. J. Jiang, J. Q. Jiang, P. W. Han, L. Dang, M. C. Xu, M. Shao, F. He, and Q. H. Wu, *Joule*, **5**, 931 (2021).
(9) J. Roncali and I. Grosu, *Adv. Sci.*, **6**, 1801026 (2019).
(10) Y. He, N. Li, and C. J. Brabec, *Org. Mater.*, **3**, 228 (2021).
(11) G. U. Kim, Y. W. Lee, B. S. Ma, J. Kim, J. S. Park, S. Lee, T. L. Nguyen, M. Song, T. S. Kim, H. Y. Woo, and B. J. Kim, *J. Mater. Chem. A*, **8**, 13522 (2020).
(12) W. Y. Yang, Z. H. Luo, R. Sun, J. Guo, T. Wang, Y. Wu, W. Wang, J. Guo, Q. Wu, M. M. Shi, H. N. Li, C. L. Yang, and J. Min, *Nat. Commun.*, **11**, 1218 (2020).
(13) S. Izawa, K. Hashimoto, and K. Tajima, *Phys. Chem. Chem. Phys.*, **14**, 16138 (2012).
(14) J. A. Bartelt, Z. M. Beiley, E. T. Hoke, W. R. Mateker, J. D. Douglas, B. A. Collins, J. R. Tumbleston, K. R. Graham, A. Amassian, H. Ade, J. M. J. Frechet, M. F. Toney, and M. D. McGehee, *Adv. Energy. Mater.*, **3**, 364 (2013).
(15) H. Cha, J. Q. Li, Y. F. Li, S. O. Kim, Y. H. Kim, and S. K. Kwon, *Macromol. Res.*, **28**, 820 (2020).
(16) X. D. Jiang, J. J. Yang, S. Karuthedath, J. Y. Li, W. N. Lai, C. Li, C. Y. Xiao, L. Ye, Z. F. Ma, Z. Tang, F. Laquai, and W. W. Li, *Angew. Chem., Int. Ed.*, **59**, 21683 (2020).
(17) Y. Wu, J. Guo, W. Wang, Z. H. Chen, Z. Chen, R. Sun, Q. Wu, T. Wang, X. T. Hao, H. M. Zhu, and J. Min, *Joule*, **5**, 1800 (2021).
(18) S. Y. Li, X. Yuan, Q. L. Zhang, B. Li, Y. X. Li, J. G. Sun, Y. F. Feng, X. N. Zhang, Z. Wu, H. Wei, M. Wang, Y. Y. Hu, Y. Zhang, H. Y. Woo, J. Y. Yuan, and W. L. Ma, *Adv. Mater.*, **33**, 2101295 (2021).
(19) C. G. Park, S. H. Park, Y. Kim, T. L. Nguyen, H. Y. Woo, H. Kang, H. J. Yoon, S. Park, M. J. Cho, and D. H. Choi, *J. Mater. Chem. A*, **7**, 21280 (2019).
(20) S. H. Park, Y. Kim, N. Y. Kwon, Y. W. Lee, H. Y. Woo, W. S. Chae, S. Park, M. J. Cho, and D. H. Choi, *Adv. Sci.*, **7**, 1902470 (2020).
(21) C. Li, X. X. Wu, X. Y. Sui, H. B. Wu, C. Wang, G. T. Feng, Y. G. Wu, F. Liu, X. F. Liu, Z. Tang, and W. W. Li, *Angew. Chem., Int. Ed.*, **58**, 15532 (2019).
(22) F. Pierini, M. Lanzi, P. Nakielski, S. Pawlowska, O. Urbanek, K. Zembrzycki, and T. A. Kowalewski, *Macromolecules*, **50**, 4972 (2017).
(23) A. Cravino and N. S. Sariciftci, *J. Mater. Chem.*, **12**, 1931 (2002).
(24) G. T. Feng, J. Y. Li, F. J. M. Colberts, M. M. Li, J. Q. Zhang, F. Yang, Y. Z. Jin, F. L. Zhang, R. A. J. Janssen, C. Li, and W. W. Li, *J. Am. Chem. Soc.*, **139**, 18647 (2017).
(25) W. B. Lai, C. Li, J. Q. Zhang, F. Yang, F. J. M. Colberts, B. Guo, Q. M. Wang, M. M. Li, A. D. Zhang, R. A. J. Janssen, M. J. Zhang, and W. W. Li, *Chem. Mater.*, **29**, 7073 (2017).
(26) C. Li, C. S. Yu, W. B. Lai, S. J. Liang, X. D. Jiang, G. T. Feng, J. Q. Zhang, Y. H. Xu, and W. W. Li, *Macromol. Rapid Commun.*, **39**, 1700611 (2018).
(27) G. T. Feng, J. Y. Li, Y. K. He, W. Y. Zheng, J. Wang, C. Li, Z. Tang, A. Osvet, N. Li, C. J. Brabec, Y. P. Yi, H. Yan, and W. W. Li, *Joule*, **3**, 1765 (2019).

(28) F. Yang, J. Y. Li, C. Li, and W. W. Li, *Macromolecules*, **52**, 3689 (2019).
(29) P. T. Yu, G. T. Feng, J. Y. Li, C. Li, Y. H. Xu, C. Y. Xiao, and W. W. Li, *J. Mater. Chem. C*, **8**, 2790 (2020).
(30) W. Wang, R. Sun, J. Guo, J. Guo, and J. Min, *Angew. Chem., Int. Ed.*, **58**, 14556 (2019).
(31) T. L. Nguyen, T. H. Lee, B. Gautam, S. Y. Park, K. Gundogdu, J. Y. Kim, and H. Y. Woo, *Adv. Funct. Mater.*, **27**, 1702474 (2017).
(32) K. Narayanaswamy, A. Venkateswararao, P. Nagarjuna, S. Bishnoi, V. Gupta, S. Chand, and S. P. Singh, *Angew. Chem., Int. Ed.*, **55**, 12334 (2016).
(33) S. Lucas, T. Leydecker, P. Samori, E. Mena-Osteritz, and P. Bauerle, *Chem. Commun.*, **55**, 14202 (2019).
(34) S. Lucas, J. Kammerer, M. Pfannmoller, R. R. Schroder, Y. K. He, N. Li, C. J. Brabec, T. Leydecker, P. Samori, T. Marszalek, W. Pisula, E. Mena-Osteritz, and P. Bauerle, *Sol. RRL*, **5**, 2000653 (2021).
(35) A. Aubele, Y. He, T. Kraus, N. Li, E. Mena-Osteritz, P. Weitz, T. Heumüller, K. Zhang, C. J. Brabec, and P. Bäuerle, *Adv. Mater.*, 2103573 (2021).
(36) A. Torpe and D. J. Belton, *Anal. Sci.*, **31**, 125 (2015).
(37) M. J. Kim, Y. W. Lee, Y. Lee, H. Y. Woo, and J. H. Cho, *J. Mater. Chem. C*, **6**, 5698 (2018).
(38) M. A. Uddin, T. H. Lee, S. Xu, S. Y. Park, T. Kim, S. Song, T. L. Nguyen, S. J. Ko, S. Hwang, J. Y. Kim, and H. Y. Woo, *Chem. Mater.*, **27**, 5997 (2015).
(39) B. Z. Xia, K. Lu, L. Yuan, J. Q. Zhang, L. Y. Zhu, X. W. Zhu, D. Deng, H. Li, and Z. X. Wei, *Polym. Chem.*, **7**, 1323 (2016).
(40) Y. H. Liu, Z. Zhang, S. Y. Feng, M. Li, L. L. Wu, R. Hou, X. J. Xu, X. B. Chen, and Z. S. Bo, *J. Am. Chem. Soc.*, **139**, 3356 (2017).
(41) Z. H. Yao, Y. K. Li, S. X. Li, J. L. Xiang, X. X. Xia, X. H. Lu, M. M. Shi, and H. Z. Chen, *ACS Appl. Energy Mater.*, **4**, 819 (2021).
(42) F. Amblard, J. H. Cho, and R. F. Schinazi, *Chem. Rev.*, **109**, 4207 (2009).
(43) P. M. Diz, A. Coelho, A. El Maatougui, J. Azuaje, O. Caamano, A. Gil, and E. Sotelo, *J. Org. Chem.*, **78**, 6540 (2013).
(44) S. Diez-Gonzalez, *Catal. Sci. Technol.*, **1**, 166 (2011).
(45) Y. W. Lee, J. Yeop, H. Lim, W.-W. Park, J. F. Joung, S. Park, O.-H. Kwon, J. Y. Kim, and H. Y. Woo, *ACS Appl. Mater. Interfaces.* (2021).
(46) K. C. Dickey, J. E. Anthony, and Y. L. Loo, *Adv. Mater.*, **18**, 1721 (2006).
(47) M. Lenes, M. Morana, C. J. Brabec, and P. W. M. Blom, *Adv. Funct. Mater.*, **19**, 1106 (2009).
(48) W. Tress, K. Leo, and M. Riede, *Phys. Rev. B*, **85** (2012).
(49) K. D. Rosenthal, M. P. Hughes, B. R. Luginbuhl, N. A. Ran, A. Karki, S. J. Ko, H. Hu, M. Wang, H. Ade, and T. Q. Nguyen, *Adv. Energy. Mater.*, **9**, 1901077 (2019).
(50) J. Z. Yao, T. Kirchartz, M. S. Vezie, M. A. Faist, W. Gong, Z. C. He, H. B. Wu, J. Troughton, T. Watson, D. Bryant, and J. Nelson, *Phys. Rev. Appl.*, **4**, 014020 (2015).
(51) X. N. Zhang, X. B. Zuo, S. K. Xie, J. Y. Yuan, H. Q. Zhou, and Y. Zhang, *J. Mater. Chem. A*, **5**, 17230 (2017).

